PHOTONICS Research

Visible-blind short-wavelength infrared photodetector with high responsivity based on hyperdoped silicon

Xiaodong Qiu,[1] Zijing Wang,[1] Xiaotong Hou,[1] Xuegong Yu,[1,2] and Deren Yang[1,3]

[1]State Key Laboratory of Silicon Materials and School of Materials Science and Engineering, Zhejiang University, Hangzhou 310027, China
[2]e-mail: yuxuegong@zju.edu.cn
[3]e-mail: mseyang@zju.edu.cn

Received 21 November 2018; revised 15 January 2019; accepted 21 January 2019; posted 23 January 2019 (Doc. ID 352296); published 28 February 2019

Developing a low-cost, room-temperature operated and complementary metal-oxide-semiconductor (CMOS) compatible visible-blind short-wavelength infrared (SWIR) silicon photodetector is of interest for security, telecommunications, and environmental sensing. Here, we present a silver-supersaturated silicon (Si:Ag)-based photodetector that exhibits a visible-blind and highly enhanced sub-bandgap photoresponse. The visible-blind response is caused by the strong surface-recombination-induced quenching of charge collection for short-wavelength excitation, and the enhanced sub-bandgap response is attributed to the deep-level electron-traps-induced band-bending and two-stage carrier excitation. The responsivity of the Si:Ag photodetector reaches 504 mA · W^{-1} at 1310 nm and 65 mA · W^{-1} at 1550 nm under −3 V bias, which stands on the stage as the highest level in the hyperdoped silicon devices previously reported. The high performance and mechanism understanding clearly demonstrate that the hyperdoped silicon shows great potential for use in optical interconnect and power-monitoring applications.

https://doi.org/10.1364/PRJ.7.000351

1. INTRODUCTION

Silicon-based photodetectors are low-cost and compatible with complementary metal-oxide-semiconductor (CMOS) circuits, which have strong potential to be used in the fields of integrated optics and microelectronics [1–8]. However, because silicon has an indirect bandgap with an energy of 1.12 eV, it is not traditionally considered as a suitable candidate for short-wavelength infrared (SWIR) photon detection. This is a severe barrier against the application of silicon in photonics. Many efforts have been devoted to extending the infrared response of silicon materials for the fabrication of all-silicon photodetectors based on different physical principles, including two-photon absorption [9–12], surface state absorption [13–15], internal photoemission absorption [16–18], and mid-bandgap absorption [19–21].

Moreover, it is also important to develop an SWIR photodetector with high discrimination and visible-blind in many unique applications, especially for the IR detections in the circumstance of solar radiation. The visible-blind photodetector can exclude the background noise induced by the significant and undesirable visible response, which is suitable for medicine, communication, intelligent monitoring, and military applications [22–25]. Thus far, there are no reports of visible-blind and SWIR-sensitive photodetectors fabricated with silicon materials because almost all silicon optoelectronic devices would inevitably absorb the visible light. Even though a visible-blind NIR nanocomposite photodetector could be achieved by using polymer-fullerene, lead sulfide (PbS), quantum dots (QDs) as an absorbing layer [22], such a device suffers from high-cost manufacture, a complicated fabrication process, and incompatibility with mature Si-based CMOS circuits.

In recent years, a new method, so-called hyperdoping of silicon, has attracted intensive interest in fabricating high-performance all-silicon IR photodetectors [21,26–29]. The working principle of this type of infrared photodetector is based on the mid-bandgap absorption. The incorporation of supersaturated dopants in silicon can simultaneously introduce a large density of electronic states within the forbidden bandgap, most likely producing an intermediate impurity band, responsible for sub-bandgap photon absorption [3,29–39]. The chalcogen (S, Se, Te) represents the most investigated class of hyperdopants thus far, which can exhibit a broad absorption spectrum up to about 5900 nm wavelength (corresponding to a photon energy of 0.21 eV) [40]. Despite the enhanced sub-bandgap light absorption, few results of the SWIR photoresponse based on the chalcogen hyperdoped silicon have been reported. By compensating

by acceptor dopants, e.g., boron (B), a room-temperature infrared response ($\lambda = 1550$ nm) for sulfur-hyperdoped silicon (Si:S) photodetectors has been achieved. However, this additional doping process increases the technology complexity and the cost of device fabrication.

Alternatively, some transition metals such as gold (Au) [21], titanium (Ti) [27], and nickel (Ni) [26] have also been used as the hyperdopants in silicon to realize the SWIR response. For the Si:Au photodetector, the room-temperature external quantum efficiency (EQE) was reported to be 10^{-4}–10^{-5} for 1310 and 1550 nm wavelengths at a 5 V reverse bias [21]. Recently, silver (Ag) was reported to be a more suitable candidate of hyperdopants for optoelectronic applications in silicon by theoretical calculation [41]. We have previously reported a highly sensitive Si:Ag photodetector, which shows potential application in the high photoconductive gain [3]. However, the device not only exhibits weak SWIR photoresponse but also is strongly interfered by the visible noise. Thus, it is necessary to achieve a visible-blind SWIR response with high responsivity based on hyperdoped silicon from the viewpoint of practical application.

In this paper, we report a room-temperature SWIR photodetector based on silver-hyperdoped silicon (Si:Ag) by a high-fluence femtosecond laser-melting (fs-PLM) technology. Denser surface traps have been introduced in the hyperdoped layer. The detector exhibits a visible-blind and electron-trap-enhanced sub-bandgap photoresponse. The visible-blind response arises from the strong surface recombination-induced quenching of charge collection for short wavelengths, and the enhanced SWIR response arises from the bulk electron-traps-induced band-bending and two-stage carrier excitation. These results are of great significance for the practical use of the hyperdoped silicon in short-IR optical interconnect and power-monitoring devices.

2. EXPERIMENT

We prepared the Si:Ag samples by combining ion implantation and femtosecond laser melting. P-type single-side polished 8 mm × 8 mm silicon (100) wafers with a thickness of 500 μm and resistivity of 1–10 Ω · cm were ultrasonically cleaned in deionized (DI) water for 30 min, followed by immersing into 10% HF solution for 2 min. After that, they were first implanted with Ag ions at 190 keV to a dose of 3×10^{15} atoms/cm^2. The implants were performed at room temperature with a tilt angle of ~7° off the incident beam axis to minimize the channeling effect. Subsequently, the samples were irradiated in air with 1 kHz Ti:sapphire laser pulses (130 fs duration, 800 nm wavelength) at a fluence of 2.4 J · cm^{-2} using four shots per area.

We fabricated the photodetectors with the Si:Ag samples. Prior to electrode deposition, the Si:Ag samples were annealed in a quartz furnace at 950°C for 30 min in flowing nitrogen to effectively annihilate the thermal damages during the fs-PLM process and electrically activate the silver dopants, and then they were immersed into 10% HF solution for 2 min to remove surface oxide. A shadow-masked Ti/Au (5/100 nm) layer, which defined a 7 mm × 7 mm photosensitive area, was deposited atop the Si:Ag layer as the cathode by thermal evaporation, and the In/Ga eutectic layer was used to form an ohmic contact at the silicon backsides.

The Ag concentration profiles were characterized using the SIMS measurements by a Cameca IMS 4f SIMS instrument in Evans Materials Technology (Shanghai) Co., Ltd. Transmittance (T_r) and reflectance (R_f) of the Si:Ag samples and reference silicon were measured with a Hitachi U-4100 UV-Vis-NIR spectrophotometer equipped with an integrating sphere detector with the wavelength range of 325–1800 nm, and the absorptance (A_b) was quantified by $A_b = 1 - T_r - R_f$. The crystalline form was characterized by Raman spectra. The electrical properties of the Si:Ag layer were measured with a Hall measurement system (Lakeshore 7604), and the Si:Ag sample was prepared on a high-resistivity FZ-Si. DLTS measurements were used to identify the location and density of the deep-level trap states with a PhysTech Fourier transform DLTS system (PhysTech FT1030, 1 MHz) equipped with a helium cryostat. The Keithley 2400 source meter was used to measure the current–voltage characteristics in the dark and under illumination, respectively. The EQE spectra were measured by the PV Measurements Inc. (U.S.) QEX10 system with the frequency of 100 Hz, which was calibrated with a NIST-certified Si photodiode and Ge photodiode. The transient response speed was measured by biasing the device at −3.0 V and exposing it to a chopper-generated short pulse (800 Hz) monochromatic light, and the transient photocurrent was recorded by an oscilloscope.

3. RESULTS AND DISCUSSION

A. Characterization of Si:Ag Samples

Figure 1(a) pictorially presents the fabrication process of a Si:Ag sample, which consists of ion implantation and femtosecond laser melting. Note that the fs-laser fluence used here is higher than the previously reported one, which means that a large density of thermal-induced defects may be introduced at the surface. Figure 1(b) shows the silver concentration profiles of the samples after the ion implantation (simulated by stopping and range of ions in matter) and after the fs-PLM & 950°C annealing process (measured by time-of-flight secondary ion mass spectroscopy), respectively. The ion implantation can produce a supersaturated layer with the maximum Ag concentration of 6.75×10^{20} cm^{-3} at the depth of 60 nm. However, the ion implantation technology is a cramming doping method, which usually introduces a large density of vacancies, dislocations, and interstitial atoms or complexes into the silicon lattice. From the Raman spectra in Fig. 1(c), the doping layer is seriously damaged and almost becomes entirely amorphous after the silver implantation. The crystallinity can be partly reestablished by the subsequent fs-PLM processing, which rapidly melts the amorphous implanted layer and triggers the amorphous layer into a quasi-single crystal phase with a supersaturated dopant concentration. Therefore, the Raman signal of the sample subjected to the fs-PLM processing could be decomposed into two parts: the single crystal silicon phase (at 520 cm^{-1}) and the amorphous silicon phase (a shoulder peak on the left side of 520 cm^{-1}). The following furnace annealing can further eliminate the defects and dislocations in the hyperdoped layer and recover the damaged silicon lattice. After the 950°C annealing, the Raman signal of the single crystal silicon is significantly enhanced, indicating that the crystal lattice

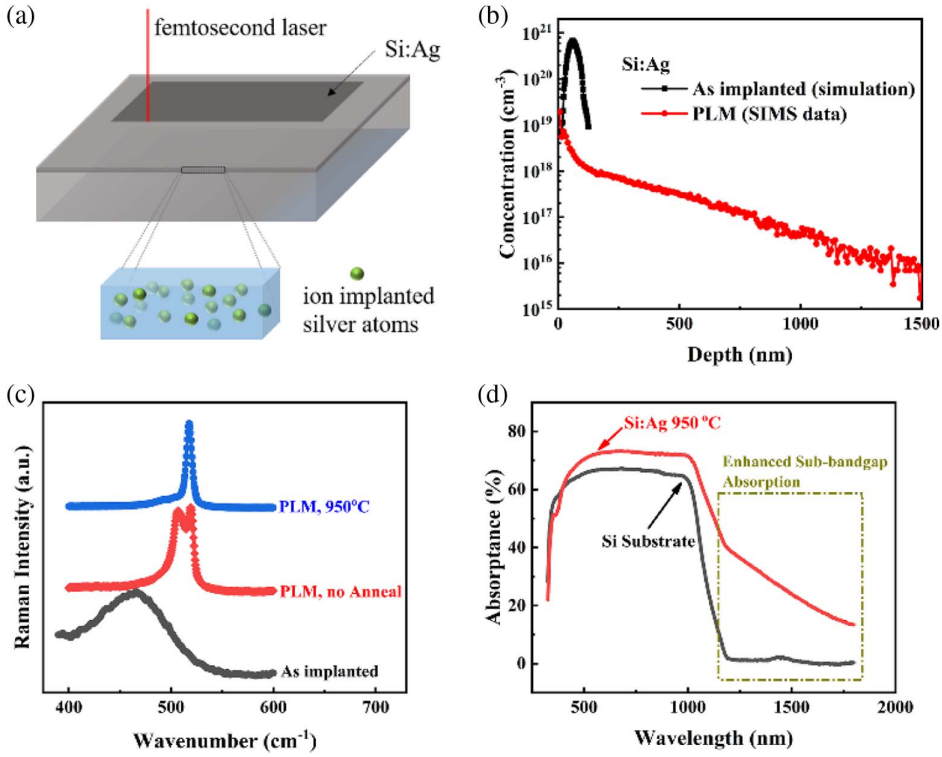

Fig. 1. (a) Fabrication diagram of a Si:Ag sample. (b) Simulation and SIMS data of the silver concentration depth profiles after the ion implantation and after the PLM. (c) The Raman spectra of the Si:Ag samples after the ion implantation and after the PLM. For the samples after PLM, the spectra with and without 950°C annealing are both shown. (d) Spectral absorptance (1-transmittance-reflectance) of the Si:Ag samples after 950°C annealing. The absorptance of the silicon substrate is also shown for comparison.

of the Si:Ag layer tends to be more ordered. The equilibrium solid-solubility limit of silver in silicon at room temperature and 950°C is less than 10^{15} cm^{-3} and 10^{18} cm^{-3}, respectively [42,43]. As shown in Fig. 1(b), the Ag concentration is about 2.0×10^{19} cm^{-3} near the surface after the fs-PLM and thermal annealing, which remains above the room-temperature solubility limit to a distance of 1.5 μm. Hall measurement confirmed that the majority carriers in the Si:Ag layer were electrons after the fs-PLM and 950°C annealing.

Figure 1(d) presents the spectral absorptance of the Si:Ag samples from 325 to 1800 nm wavelength, and conventional silicon is used as a reference sample here. Compared with the conventional silicon, the Si:Ag sample exhibits greatly enhanced optical absorption in the sub-bandgap range. This phenomenon has also been reported in our previous work, and the enhancement of the infrared light absorption is proven to arise from the intermediate energy levels induced by the supersaturated Ag dopants [3]. We have also thinned the silicon substrate to a different thickness and compared the transmittance from 325 to 1800 nm wavelength. The transmittance has barely changed for the Si:Ag samples with different substrate thicknesses, which confirms that almost all of the incident photons are absorbed by the upper layer of Si:Ag samples.

B. Optoelectronic Properties of the Fabricated Si:Ag Photodetector

The device diagram of the Si:Ag photodetector is schematically presented in Fig. 2(a). The EQE spectra were measured under different reverse biases from 0 V to −3 V with a voltage step of 0.5 V, and the results are presented in Fig. 2(b). It can be seen that the EQE spectra exhibit a visible-blind photoresponse with only a single narrow peak (∼1120 nm) near the absorption edge of Cz-Si, which is greatly distinguished from the wide absorption spectra shown in Fig. 1(d). The EQE values of the Si:Ag photodetector increased monotonically with the reverse bias, and the maximum EQE value exceeded 100% at −1.5 V bias, indicating a photoconductive gain. It should also be noted that there is an obvious kink in the EQE spectra at around 1180 nm wavelength, which is in good agreement with the spectral absorptance result in Fig. 1(d). For the wavelength above 1180 nm, the declining trend of EQE spectra obviously slows down, and the spectral response can even extend to the wavelength of 1600 nm. As shown in Fig. 2(c), the EQE values can reach 47.78% and 5.19% for the wavelengths of 1310 and 1550 nm, corresponding to the responsivity (R, defined as the ratio of photocurrent to the power of incident irradiation) of 504 mA · W^{-1} and 65 mA · W^{-1}, respectively. These values, to our knowledge, represent the highest response level in the previously reported hyperdoped silicon photodetectors, more than 2 orders of magnitude higher than the results in the Si:Au [21] and Si:Se [28] photodetectors. Figure 2(d) shows the current density-voltage (J–V) curves of the Si:Ag photodetector in the dark and under the 1310 nm infrared light illumination (0.60 mW · cm^{-2}). The photocurrent exhibited a clear trend of increase with the reverse bias, corresponding well with the EQE variation in Fig. 2(b), which further

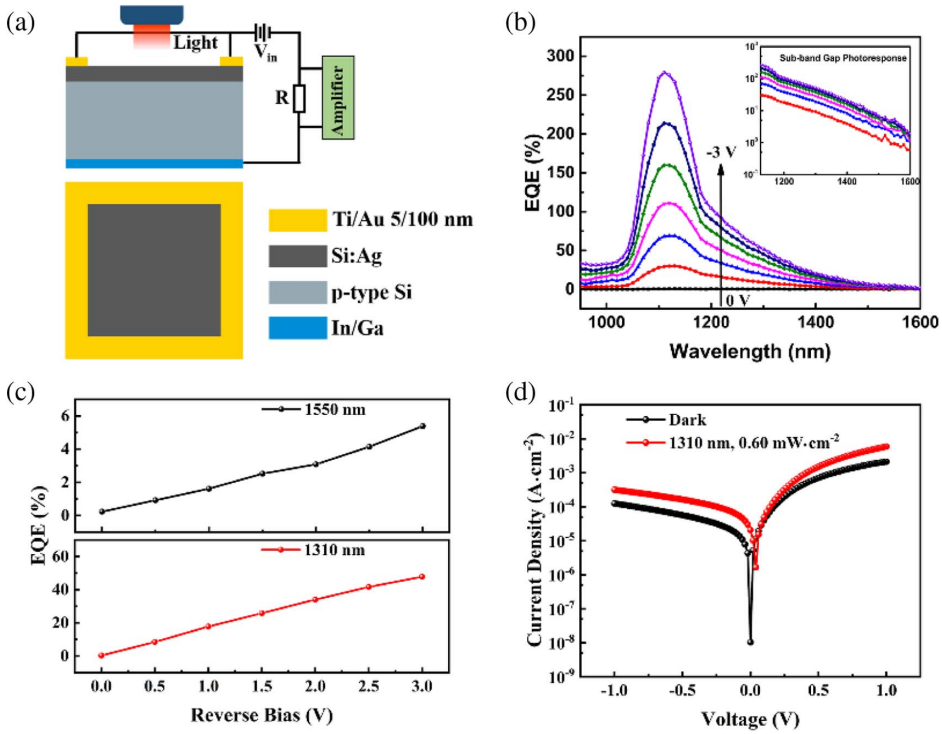

Fig. 2. (a) Schematic diagram of fabricated photodetector device components. (b) EQE spectra (900–1600 nm) of the Si:Ag photodetector under reverse bias from 0 V to −3 V with an interval of 0.5 V. (c) EQE increases with the applied reverse bias for 1310 nm and 1550 nm, respectively. (d) The current density-voltage curves of the Si:Ag photodetector in the dark and under the 1310 nm infrared light illumination (0.6 mW · cm^{-2}).

confirms that the device works as a photoconductor under illumination.

The deep-level transient spectroscopy (DLTS) measurement was further used to characterize the deep levels induced by ultrahigh doping. The reverse bias voltage (V_R) was varied from −3 to −5 V; meanwhile, the filling pulse voltage (V_P) was set as −1 V to distinguish the surface traps and the bulk traps within the silicon forbidden band. The DLTS results are presented in Fig. 3(a). For a surface trap state, the DLTS signal should be directly determined by the energy distribution within the energy window between the Fermi levels at the surface for the quiescent pulse voltage (V_P) and bias voltage (V_R). Because the surface trap states are distributed with a relatively wider energy range in the forbidden bandgap, the peak temperature for the surface trap signal is variable with the bias voltage. On the contrary, for a bulk trap with a discrete energy distribution, the emission rate is a constant regardless of the bias voltage, so the peak temperature cannot be changed [44]. In Fig. 3(a), there are two peaks in the DLTS spectra, which are correspondingly designated as T1 and T2. The peak of the T2 level shifts toward low temperature with an increase of reverse bias voltage, which reflects the characteristics of the surface trap states. These surface charge traps could act as the surface nonradiative recombination centers for the photoexcited carriers in the Si:Ag photodetectors and influence the optoelectronic performance. We further compared the peak intensity of the T2 level of the Si:Ag samples subjected to different fs-laser fluences in Fig. 3(b). The density of T2 trap states exhibits a conspicuous monotonic

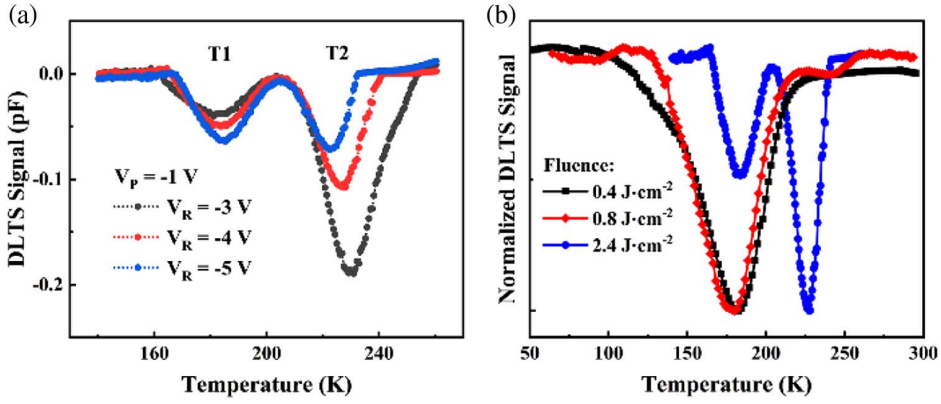

Fig. 3. (a) DLTS spectra of the Si:Ag MOS diode for the reverse bias voltage of −3 V, −4 V, and −5 V, respectively. The pulse voltage was set as −1 V. (b) Normalized DLTS signals of the Si:Ag samples subjected to different energy fluence fs-PLM processing.

increase with the laser fluences, indicating that these surface traps might be induced by the thermal effects during the fs-PLM process. For the T1 level, the peak temperature does not shift with the bias voltage, which originates from bulk trap states. Based on the Arrhenius plots, the activation energy of 0.32 eV and the capture cross-section of 8.1×10^{-16} cm^2 can be derived for the T1 level, which is consistent with substitutional Ag-atoms-induced electron trap states, as we have previously reported [3]. Generally, the existence of the large density of surface and bulk charge traps should have a remarkable influence on the photoresponse of the Si:Ag photodetectors.

The high densities of surface traps observed by the DLTS spectra lead us to believe that the strong surface recombination could account for the visible-blind spectral photoresponse. Figure 4(a) illustrates the mechanism for the differentiated response performance in the above- and sub-bandgap range. For a normal photodetector, the responsivity should be determined by not only the optical absorptance but also by the charge collection efficiency [22,24,45,46]. With the existence of dense trap states, the charge collection efficiency for the Si:Ag photodetector should be strongly dependent on the light wavelength. For shorter wavelength (λ_1) photoexcitation, the Si:Ag is an optically active but electronically dead layer. Due to the large absorption coefficient (i.e., short penetration depth, L_p), photogenerated carriers are generally distributed close to the upper surface of the Si:Ag layer. These charge carriers could be easily quenched by the strong surface recombination, and almost no charges could transport across the entire Si:Ag layer and be collected by the back contact. Thus, the devices almost have no response in the visible range, as shown in Fig. 4(b). Conversely, for SWIR wavelength (λ_2) photoexcitation, light could penetrate much deeper into the Si:Ag layer due to the much weaker absorption coefficient, and the photogenerated charges have fewer possibilities to be surface-recombined. These free carriers could be effectively extracted under the applied reverse bias and then be collected by electrode to yield the photocurrent. Therefore, these surface traps should have hardly any influence on the long-wavelength light photoresponse. As a result, the photoresponse to long-wavelength light is much greater compared with the short-wavelength light in Fig. 4(b). We have also compared the normalized EQE spectra ranging from 300 to 1600 nm based on the Si:Ag devices subjected to different fs-laser fluences, and the results are presented in Fig. 4(c). As reported in the sulfur hyperdoped silicon (Si:S) photodetector, the responsivity narrows and shifts toward a longer wavelength with increasing laser fluence [47], which has also been observed in the Si:Ag photodetectors. As the density of charge traps increases monotonically with laser fluences [presented in Fig. 3(b)], the EQE spectra present a clear trend of narrowing effect when subjected to a higher-fluence fs-PLM, which is in good correspondence with our hypothesis.

The working principle of the Si:Ag photodetector for the sub-bandgap light detection is pictorially presented in Fig. 5. Because the supersaturated silver atoms in the silicon lattice can produce a high density of deep-level electron trap states, they can act as a transition level for the sub-bandgap photogenerated carrier excitation. For photons with energy E_{ph} exceeding $E_g - \Delta E_i$, electrons exciting from both the valence band to the impurity states and from the impurity states to the conduction band are realizable. Due to the relatively smaller absorption coefficient and larger penetration depth, these photogenerated carriers could eventually be extracted by the metal contacts under reverse bias to generate considerable photocurrent. Besides, under SWIR illumination, this transition level might be occupied by the photogenerated electrons, which would cause the lowest unoccupied molecular orbital (LUMO) of the silicon to downward shift, and the energy band to dramatically bend at the Ti/Au cathode side. As a result, the hole injection barrier could be significantly reduced, and holes could easily tunnel through it from the Ti/Au cathode under a small reverse bias. By increasing the reverse bias and light illumination intensity, the hole injection would be more frequent, and the quantity of the injected holes can far surpass the photogenerated ones, which means a large response gain can be observed in the Si:Ag photodetectors. As a summary, due to the transition-level-assisted extrinsic sub-bandgap absorption and external hole tunneling, the SWIR response of our Si:Ag photodetectors can be significantly enhanced compared with the commercially used silicon photodetectors.

C. Performance of the Si:Ag Photodetector

The transient response of the Si:Ag photodetector has been characterized by exposing the detector to an 800 Hz chopped 1310 nm monochromatic light and recording the transient photocurrent with an oscilloscope. Figure 6(a) presents the transient result measured under −3.0 V reverse bias with the light intensity of 0.60 $mW \cdot cm^{-2}$. We fit the photocurrent transient rise behavior to a double-exponential model and

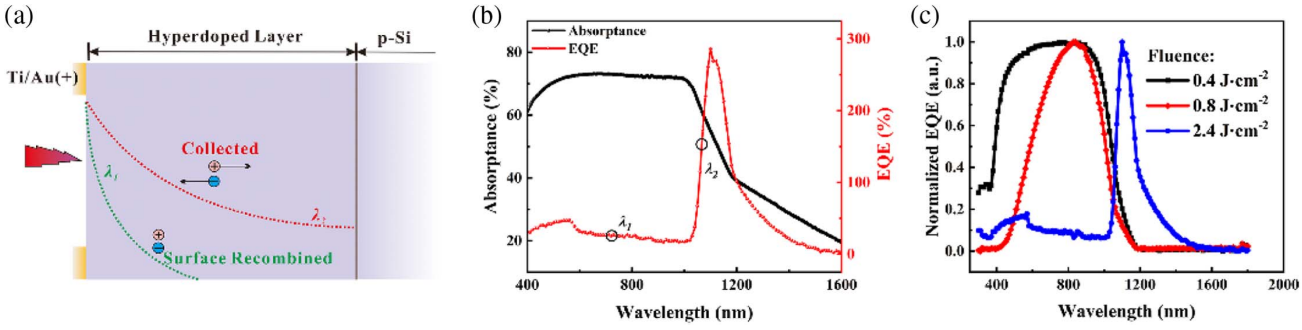

Fig. 4. (a) Illustration of the vilible-blind photodetector working mechanism. (b) Spectral absorptance and EQE of the Si:Ag photodetector. (c) Effect of the fs-laser fluence on the normalized EQE spectra (300–1800 nm) of the Si:Ag photodetectors.

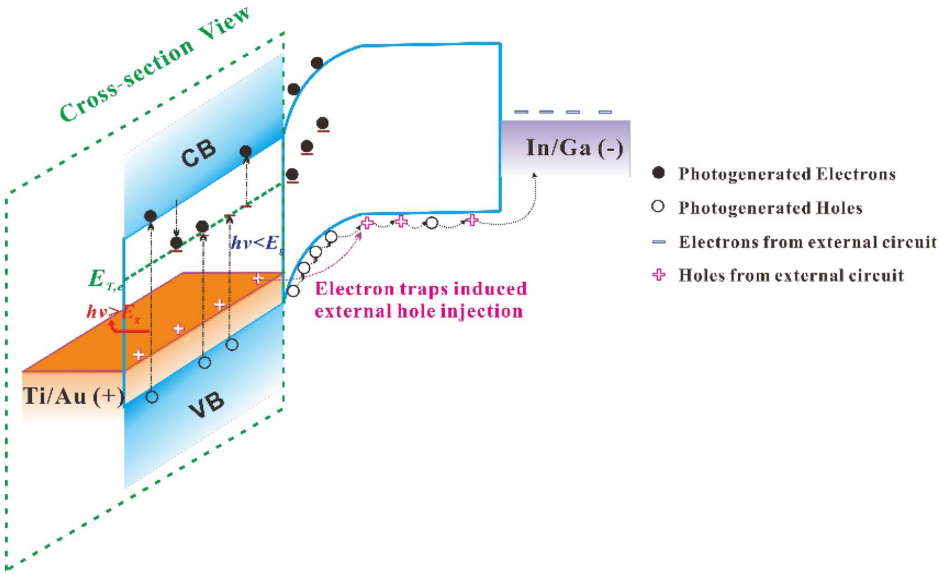

Fig. 5. Illustration of the sub-bandgap and high-gain photoresponse working mechanism.

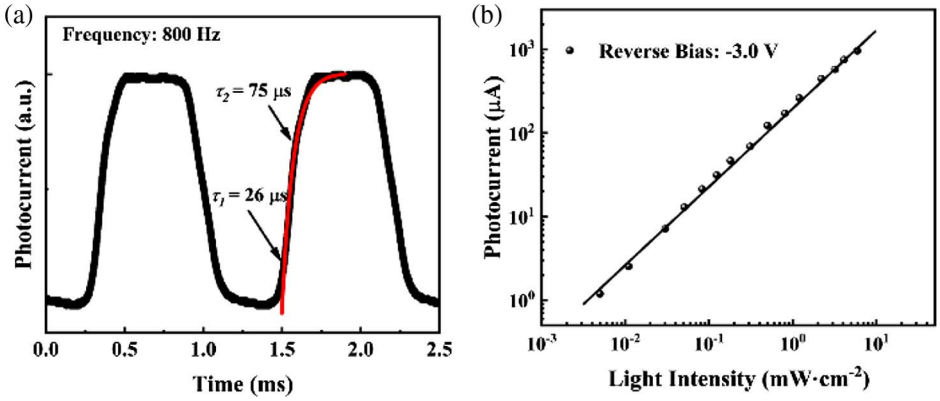

Fig. 6. (a) Transient photocurrent of the Si:Ag photodetector measured at −3 V under 1310 nm light illumination. (b) Net photocurrent versus incident photon intensity for 1310 nm wavelength.

obtained a faster component of 26.3 ± 5.9 μs and a slower component of 75.4 ± 1.6 μs, respectively. The rise behavior of the photocurrent should arise from multiple steps such as sub-bandgap photon absorption, deep-level state-assisted electron transition, charge trapping, energy band bending, and hole injection. Among these steps, the charge-trapping step may dominate the photocurrent rise behavior because all other processes should be much faster [48,49]. The bi-exponential rise of the photocurrent probably arises from different trapping mechanisms for photogenerated carriers because of the existence of bulk and surface traps. The time constants for these two trapping processes should be distinguished due to the different trap depths. The decay time (photocurrent signal changing from 90% to 10% of the peak value) of the Si:Ag photodetector was directly extracted to be 179 μs. We can further calculate the photoconductive gain of the detector using the ratio of carrier recombination time (or device switch-off time) and transmit time by

$$G = \frac{\tau_{\text{fall}}}{t_{\text{transimittime}}} = \frac{\tau_{\text{fall}}}{d^2/\mu V}, \quad (1)$$

where d is the device thickness, μ is the hole mobility, and V is the applied reverse-bias voltage. Here, the photoconductive gain was calculated to be approximately 107.4 at −3.0 V reverse bias. Figure 6(b) presented the photocurrent of the Si:Ag photodetector as a function of the input light intensity at 1310 nm measured at −3.0 V. The device shows a linear response within the light intensity ranging from 5.0 μW · cm^{-2} to 5.9 mW · cm^{-2}, and this linear relationship confirmed that the sub-bandgap photoresponse of our device was caused by the dopant states' mediated single-photon absorption rather than the two-photon absorption [21,28].

4. CONCLUSION

In summary, we have demonstrated a room-temperature visible-blind SWIR photodetector based on the silver-hyperdoped silicon (Si:Ag), which is prepared by means of ion implantation and femtosecond laser melting. A large density of electron traps was introduced both on the surface and within the hyperdoped layer. The strong surface recombination-induced quenching of

charge collection for short-wavelength leads to the visible-blind photodetection, and the bulk electron-traps-induced band-bending and two-stage carrier excitation cause the enhanced sub-bandgap photoresponse. The photoresponse of the Si:Ag photodetector could be extended to the wavelength of 1600 nm, and the room-temperature responsivity of 504 $mA \cdot W^{-1}$ at 1310 nm and 65 $mA \cdot W^{-1}$ at 1550 nm was obtained. The high performance and mechanism understanding open up the possibility of using the Si:Ag photodetector in the current optoelectronics. From the viewpoint of practical application, design of the photodetector array should be included in future work, in which the contact geometry and doping homogeneity need to be well controlled.

Funding. National Natural Science Foundation of China (NSFC) (51532007, 61574124, 61721005).

Acknowledgment. The authors acknowledge the facilities and the scientific and technical assistance of the Suzhou Delphi Laser Co., Ltd.

REFERENCES

1. T. Yu, F. Wang, Y. Xu, L. Ma, X. Pi, and D. Yang, "Graphene coupled with silicon quantum dots for high-performance bulk-silicon-based Schottky-junction photodetectors," Adv. Mater. **28**, 4912–4919 (2016).
2. X. Wang, Z. Cheng, K. Xu, H. K. Tsang, and J.-B. Xu, "High-responsivity graphene/silicon-heterostructure waveguide photodetectors," Nat. Photonics **7**, 888–891 (2013).
3. X. Qiu, X. Yu, S. Yuan, Y. Gao, X. Liu, Y. Xu, and D. Yang, "Trap assisted bulk silicon photodetector with high photoconductive gain, low noise, and fast response by Ag hyperdoping," Adv. Opt. Mater. **6**, 1700638 (2018).
4. Z. Huang, J. E. Carey, M. Liu, X. Guo, E. Mazur, and J. C. Campbell, "Microstructured silicon photodetector," Appl. Phys. Lett. **89**, 033506 (2006).
5. M. Casalino, L. Sirleto, L. Moretti, M. Gioffrè, G. Coppola, and I. Rendina, "Silicon resonant cavity enhanced photodetector based on the internal photoemission effect at 1.55 m: fabrication and characterization," Appl. Phys. Lett. **92**, 251104 (2008).
6. D.-S. Tsai, C.-A. Lin, W.-C. Lien, H.-C. Chang, Y.-L. Wang, and J.-H. He, "Ultra-high-responsivity broadband detection of Si metal-semiconductor-metal Schottky photodetectors improved by ZnO nanorod arrays," ACS Nano **5**, 7748–7753 (2011).
7. X. Li, J. Carey, J. Sickler, M. Pralle, C. Palsule, and C. Vineis, "Silicon photodiodes with high photoconductive gain at room temperature," Opt. Express. **20**, 5518–5523 (2012).
8. Z. Chen, Z. Cheng, J. Wang, X. Wan, C. Shu, H. K. Tsang, H. P. Ho, and J. B. Xu, "High responsivity, broadband, and fast graphene/silicon photodetector in photoconductor mode," Adv. Opt. Mater. **3**, 1207–1214 (2015).
9. J. F. Reintjes and J. C. McGroddy, "Indirect two-photon transitions in Si at 1.06 μm," Phys. Rev. Lett. **30**, 901–903 (1973).
10. H. K. Tsang, C. S. Wong, T. K. Liang, I. E. Day, S. W. Roberts, A. Harpin, J. Drake, and M. Asghari, "Optical dispersion, two-photon absorption and self-phase modulation in silicon waveguides at 1.5 μm wavelength," Appl. Phys. Lett. **80**, 416–418 (2002).
11. A. R. Cowan, G. W. Rieger, and J. F. Young, "Nonlinear transmission of 1.5 μm pulses through single-mode silicon-on-insulator waveguide structures," Opt. Express **12**, 1611–1621 (2004).
12. M. Dinu, F. Quochi, and H. Garcia, "Third-order nonlinearities in silicon at telecom wavelengths," Appl. Phys. Lett. **82**, 2954–2956 (2003).
13. H. Chen, X. S. Luo, and A. W. Poon, "Cavity-enhanced photocurrent generation by 1.55 μm wavelengths linear absorption in a p-i-n diode embedded silicon microring resonator," Appl. Phys. Lett. **95**, 171111 (2009).
14. T. Baehr-Jones, M. Hochberg, and A. Scherer, "Photodetection in silicon beyond the band edge with surface states," Opt. Express **16**, 1659–1668 (2008).
15. M. W. Geis, S. J. Spector, M. E. Grein, R. T. Schulein, J. U. Yoon, D. M. Lennon, S. Deneault, F. Gan, F. X. Kaertner, and T. M. Lyszczarz, "CMOS-compatible all-Si high-speed waveguide photodiodes with high responsivity in near-infrared communication band," IEEE Photon. Technol. Lett. **19**, 152–154 (2007).
16. A. Akbari and P. Berini, "Schottky contact surface-plasmon detector integrated with an asymmetric metal stripe waveguide," Appl. Phys. Lett. **95**, 021104 (2009).
17. S. Y. Zhu, G. Q. Lo, M. B. Yu, and D. L. Kwong, "Low-cost and high-gain silicide Schottky-barrier collector phototransistor integrated on Si waveguide for infrared detection," Appl. Phys. Lett. **92**, 081103 (2008).
18. M. Casalino, L. Sirleto, M. Iodice, N. Saffioti, M. Gioffre, I. Rendina, and G. Coppola, "Cu/p-Si Schottky barrier-based near infrared photodetector integrated with a silicon-on-insulator waveguide," Appl. Phys. Lett. **96**, 241112 (2010).
19. A. P. Knights, J. D. B. Bradley, S. H. Gou, and P. E. Jessop, "Silicon-on-insulator waveguide photodetector with self-ion-implantation-engineered-enhanced infrared response," J. Vac. Sci. Technol. A **24**, 783–786 (2006).
20. J. Bradley, P. Jessop, and A. Knights, "Silicon waveguide-integrated optical power monitor with enhanced sensitivity at 1550 nm," Appl. Phys. Lett. **86**, 241103 (2005).
21. J. P. Mailoa, A. J. Akey, C. B. Simmons, D. Hutchinson, J. Mathews, J. T. Sullivan, D. Recht, M. T. Winkler, J. S. Williams, J. M. Warrender, P. D. Persans, M. J. Aziz, and T. Buonassisi, "Room-temperature sub-band gap optoelectronic response of hyperdoped silicon," Nat. Commun. **5**, 3011 (2014).
22. L. Shen, Y. Zhang, Y. Bai, X. Zheng, Q. Wang, and J. Huang, "A filterless, visible-blind, narrow-band, and near-infrared photodetector with a gain," Nanoscale **8**, 12990–12997 (2016).
23. Z. Guo, S. Park, J. Yoon, and I. Shin, "Recent progress in the development of near-infrared fluorescent probes for bioimaging applications," Chem. Soc. Rev. **43**, 16–29 (2014).
24. A. Armin, R. D. Jansen-van Vuuren, N. Kopidakis, P. L. Burn, and P. Meredith, "Narrowband light detection via internal quantum efficiency manipulation of organic photodiodes," Nat. Commun. **6**, 6343 (2015).
25. A. Sobhani, M. W. Knight, Y. Wang, B. Zheng, N. S. King, L. V. Brown, Z. Fang, P. Nordlander, and N. J. Halas, "Narrowband photodetection in the near-infrared with a plasmon-induced hot electron device," Nat. Commun. **4**, 1643 (2013).
26. R. Chen, B. Fan, M. Pan, Q. Cheng, and C. Chen, "Room-temperature optoelectronic response of Ni supersaturated p-type Si processed by continuous-wave laser irradiation," Mater. Lett. **163**, 90–93 (2016).
27. E. García-Hemme, R. García-Hernansanz, J. Olea, D. Pastor, A. del Prado, I. Mártil, and G. González-Díaz, "Room-temperature operation of a titanium supersaturated silicon-based infrared photodetector," Appl. Phys. Lett. **104**, 211105 (2014).
28. Y. Berencén, S. Prucnal, F. Liu, I. Skorupa, R. Hübner, L. Rebohle, S. Zhou, H. Schneider, M. Helm, and W. Skorupa, "Room-temperature short-wavelength infrared Si photodetector," Sci. Rep. **7**, 43688 (2017).
29. C. B. Simmons, A. J. Akey, J. P. Mailoa, D. Recht, M. J. Aziz, and T. Buonassisi, "Enhancing the infrared photoresponse of silicon by controlling the fermi level location within an impurity band," Adv. Funct. Mater. **24**, 2852–2858 (2014).
30. E. Pérez, H. Castán, H. García, S. Dueñas, L. Bailón, D. Montero, R. García-Hernansanz, E. García-Hemme, J. Olea, and G. González-Díaz, "Energy levels distribution in supersaturated silicon with titanium for photovoltaic applications," Appl. Phys. Lett. **106**, 022105 (2015).
31. E. Mazur, "Black silicon: engineering an intermediate band in silicon for photovoltaic applications," in *Abstracts of Papers of the American Chemical Society*, Vol. **240**, (2010).
32. C. H. Crouch, J. E. Carey, M. Shen, E. Mazur, and F. Y. Genin, "Infrared absorption by sulfur-doped silicon formed by femtosecond laser irradiation," Appl. Phys. A **79**, 1635–1641 (2004).
33. J. T. Sullivan, C. B. Simmons, J. J. Krich, A. J. Akey, D. Recht, M. J. Aziz, and T. Buonassisi, "Methodology for vetting heavily doped semiconductors for intermediate band photovoltaics: a case study in sulfur-hyperdoped silicon," J. Appl. Phys. **114**, 103701 (2013).

34. M. J. Sher and E. Mazur, "Intermediate band conduction in femtosecond-laser hyperdoped silicon," Appl. Phys. Lett. **105**, 032103 (2014).
35. I. Umezu, J. M. Warrender, S. Charnvanichborikarn, A. Kohno, J. S. Williams, M. Tabbal, D. G. Papazoglou, X.-C. Zhang, and M. J. Aziz, "Emergence of very broad infrared absorption band by hyperdoping of silicon with chalcogens," J. Appl. Phys. **113**, 213501 (2013).
36. T.-H. Her, R. J. Finlay, C. Wu, S. Deliwala, and E. Mazur, "Microstructuring of silicon with femtosecond laser pulses," Appl. Phys. Lett. **73**, 1673–1675 (1998).
37. C. Wu, C. H. Crouch, L. Zhao, J. E. Carey, R. Younkin, J. A. Levinson, E. Mazur, R. M. Farrell, P. Gothoskar, and A. Karger, "Near-unity below-band-gap absorption by microstructured silicon," Appl. Phys. Lett. **78**, 1850–1852 (2001).
38. R. Younkin, J. E. Carey, E. Mazur, J. A. Levinson, and C. M. Friend, "Infrared absorption by conical silicon microstructures made in a variety of background gases using femtosecond-laser pulses," J. Appl. Phys. **93**, 2626–2629 (2003).
39. C. H. Crouch, J. E. Carey, J. M. Warrender, M. J. Aziz, E. Mazur, and F. Y. Genin, "Comparison of structure and properties of femtosecond and nanosecond laser-structured silicon," Appl. Phys. Lett. **84**, 1850–1852 (2004).
40. M.-J. Sher, Y.-T. Lin, M. T. Winkler, E. Mazur, C. Pruner, and A. Asenbaum, "Mid-infrared absorptance of silicon hyperdoped with chalcogen via fs-laser irradiation," J. Appl. Phys. **113**, 063520 (2013).
41. J. T. Sullivan, C. B. Simmons, T. Buonassisi, and J. J. Krich, "Targeted search for effective intermediate band solar cell materials," IEEE J. Photovolt. **5**, 212–218 (2015).
42. F. Rollert, N. A. Stolwijk, and H. Mehrer, "Solubility, diffusion and thermodynamic properties of silver in silicon," J. Phys. D **20**, 1148–1155 (1987).
43. A. Fazzio, M. J. Caldas, and A. Zunger, "Electronic-structure of copper, silver, and gold impurities in silicon," Phys. Rev. B **32**, 934–954 (1985).
44. K. Yamasaki, M. Yoshida, and T. Sugano, "Deep level transient spectroscopy of bulk traps and interface states in Si MOS diodes," Jpn. J. Appl. Phys. **18**, 113–122 (1979).
45. Y. J. Fang, Q. F. Dong, Y. C. Shao, Y. B. Yuan, and J. S. Huang, "Highly narrowband perovskite single-crystal photodetectors enabled by surface-charge recombination," Nat. Photonics **9**, 679–686 (2015).
46. L. Li, Y. Deng, C. Bao, Y. Fang, H. Wei, S. Tang, F. Zhang, and J. Huang, "Self-filtered narrowband perovskite photodetectors with ultrafast and tuned spectral response," Adv. Opt. Mater. **5**, 1700672 (2017).
47. J. E. Carey, C. H. Crouch, M. Y. Shen, and E. Mazur, "Visible and near-infrared responsivity of femtosecond-laser microstructured silicon photodiodes," Opt. Lett. **30**, 1773–1775 (2005).
48. R. Dong, Y. J. Fang, J. Chae, J. Dai, Z. G. Xiao, Q. F. Dong, Y. B. Yuan, A. Centrone, X. C. Zeng, and J. S. Huang, "High-gain and low-driving-voltage photodetectors based on organolead triiodide perovskites," Adv. Mater. **27**, 1912–1918 (2015).
49. F. W. Guo, B. Yang, Y. B. Yuan, Z. G. Xiao, Q. F. Dong, Y. Bi, and J. S. Huang, "A nanocomposite ultraviolet photodetector based on interfacial trap-controlled charge injection," Nat. Nanotechnol. **7**, 798–802 (2012).